CrystEngComm

ROYAL SOCIETY OF CHEMISTRY

PAPER

View Article Online
View Journal | View Issue

Cite this: *CrystEngComm*, 2025, **27**, 155

Chiral resolution of DL-leucine *via* salifying tartaric acid derivatives†

Linlin Shi,[a] Zhiqiang Guo,[b] Xiaofang Luo,[a] Lingli Hou,[a] Hongchang Wu,[a] Ruiyu De,[a] Xin Huang,[a] Ting Wang,[a] Hongxun Hao,[a] Na Wang *[a] and Lina Zhou *[a]

Received 12th October 2024,
Accepted 26th November 2024

DOI: 10.1039/d4ce01043d

rsc.li/crystengcomm

Diastereomeric salt formation is suitable for chiral resolution of racemic compounds and is the most effective way to obtain enantiomers. At present, there are few resolution methods for DL-leucine (DL-LEU), and the corresponding mechanism of resolution has not been studied. In this study, (+)-di-1,4-toluoyl-D-tartaric acid monohydrate (D-DTTA) was selected as the ligand. Diastereomeric salts D-LEU:D-DTTA (D–D) and L-LEU:D-DTTA (L–D) were synthesized by liquid-assisted grinding and then identified by powder X-ray diffraction, thermal analysis, Fourier transform infrared spectroscopy and single crystal X-ray diffraction. Their difference in crystal structures, thermodynamic properties and intermolecular interactions showed that D–D is more stable and has lower solubility, which makes chiral resolution possible. Furthermore, the mechanism of chiral recognition was investigated, which showed that D-DTTA was more easily bound to D-LEU. Finally, the optimized resolution condition was confirmed, and the ee values of D–D and L–D reached 91.20% and −73.32% respectively by the multi-stage crystallization process. This study provides an effective and industrially applicable method for the separation of the DL-LEU racemic compound, and provides a reference for the screening of salt-forming chiral resolution agents.

Introduction

According to statistics, about 57% of the drugs sold in the market are chiral drugs.[1] Chirality is one of the most important properties in nature,[2] which is directly related to the pharmacological effects of chiral drugs. For example, *S*-ibuprofen has anti-inflammatory and analgesic effects, while *R*-ibuprofen has low pharmacological activity and may cause side effects such as stomach ulcers and liver damage.[3,4] D-Penicillamine can be used to treat rheumatoid arthritis, while L-penicillamine is toxic.[5,6] D-Propoxyphene has an analgesic effect, while L-propoxyphene is a cough suppressant.[7] Therefore, it is of great significance to obtain a single enantiomer during drug production. The main methods for obtaining enantiomers are asymmetric synthesis, chiral synthesis and chiral resolution.[8–10] However, the types of natural chiral compounds that can be used as chiral sources are limited,[11] the process route of synthesis is usually more complicated and the cost is relatively expensive.[12,13] Therefore, chiral resolution is generally used to separate the racemate into two enantiomers. The main methods of chiral resolution based on crystallization include spontaneous crystallization resolution,[14,15] diastereomeric salt formation[16] and preferential crystallization (PC).[17,18] Preferential crystallization is characterized by simplicity and great efficiency, but it is only suitable for the case of 5–10% conglomerates.[19,20] More than 90% of the racemic systems are crystalline in the form of racemic compounds, which greatly limits the development and application of chiral drugs. Therefore, the resolution of racemic compounds is very important in the fields of medicine and food. A resolution agent is often used to convert the racemic compound into a pair of diastereomeric salts/cocrystals,[21] which can be separated by the difference in chiral recognition ability.[22] For example, praziquantel (PZQ) and L-malic acid (L-MA) form diastereomeric eutectic pairs comprising *R*-PZA:L-MA and *S*-PZQ:L-MA, exploiting the stronger intermolecular interaction of *R*-PZA:L-MA to achieve chiral resolution.[23] *O*,*O*′-Dibenzoyl-(2*S*,3*S*)-tartaric acid and *O*,*O*′-dibenzoyl-(2*R*,3*R*)-tartaric acid are highly effective chiral resolution agents to separate racemic ofloxacin by the formation of eutectic pairs of diastereoisomers in the water phase.[24] However, the chiral resolution mechanism is not fully studied, and there is a lack of guiding principles for the selection of resolution agents and resolution methods.

The basic building blocks of proteins are amino acids.[25] Amino acids in life are mainly L-amino acids, which is an

[a] *National Engineering Research Center of Industrial Crystallization Technology, School of Chemical Engineering and Technology, Tianjin University, Tianjin, 300072, People's Republic of China. E-mail: wangna224@tju.edu.cn, linazhou@tju.edu.cn*
[b] *Jewim Pharmaceutical (Shandong) Co., Ltd., Shandong, 271000, People's Republic of China*

† Electronic supplementary information (ESI) available. CCDC 2387200 and 2387201. For ESI and crystallographic data in CIF or other electronic format see DOI: https://doi.org/10.1039/d4ce01043d

important factor in the origin and evolution of life. While the most non-natural amino acids are racemic, the physiological roles of D- and L-amino acids are so different that more researchers focus on chiral resolution, which is critical for drug development, biological research and other fields.[26] In this paper, DL-leucine (DL-LEU) was selected as the model compound. D-Leucine (D-LEU) and L-leucine (L-LEU) are nutritional supplements that act as chiral sources and intermediates in drug synthesis.[27] D-LEU also has antiepileptic activity.[28] Therefore, the chiral resolution of DL-LEU is of great significance for medicine, food and other fields. At present, there are few research studies on chiral resolution of DL-LEU. Ryuzo Yoshioka used (*S*)-(−)-1-phenylethanesulfonic acid to form diastereomeric salts with DL-LEU, but the resolution mechanism has not been investigated.[29] Oleksii Shemchuk prepared racemic ionic eutectic mixtures of lithium chloride and DL-LEU by methanol-assisted grinding.[30] However, it is unstable and rapidly transforms into racemic compounds. In this work, the diastereomeric salts were formed with DL-LEU by selecting a suitable resolution agent, and the thermodynamics and resolution mechanism were studied.

Experimental

Materials

DL-LEU, L-LEU, D-LEU, D-phenylalaninol (D-PPA) and (+)-di-1,4-toluoyl-D-tartaric acid monohydrate (D-DTTA) were supplied by Tianjin Heowns Biochemical Technology Co., Ltd. (Tianjin, China), with their chemical purity higher than 99%. D-Penicillamine (D-PEN) was supplied by Shanghai Meryer Chemical Technology Co., Ltd. (Shanghai, China), with its chemical purity higher than 98%. L-Ascorbic acid (L-VC), *S*-naproxen (*S*-NAP) and *S*-ibuprofen (*S*-IBU) were purchased from Shanghai Bide Pharmatech Ltd. (Shanghai, China), with their chemical purity greater than 98%. Methanol (mass purity ≥99.9%) was purchased from Tianjin Kemiou Chemical Reagent Co., Ltd. (Tianjin, China). All chemicals were used without any further purification.

Liquid-assisted grinding (LAG)

0.01 mmol DL-LEU and 0.01 mmol ligand (D-PPA, *S*-IBU, D-PEN, D-DTTA, L-VC and *S*-NAP) were added to a 2 mL centrifuge tube with one pellet of zirconia and 10 μL mixed solvents of methanol and water (MeOH/H_2O). Then a high-throughput ball mill was used to grind the sample for 40 min at a frequency of 30 Hz, and the product was dried for powder X-ray diffraction analysis to determine whether a new phase was formed. If DL-LEU forms a new phase with a ligand, D-/L-LEU is then ground with this ligand according to the above steps (Fig. 1).

Characterization and determination

Powder X-ray Diffraction (PXRD). To determine the component and crystal forms of monomers and multi-component crystals, PXRD patterns were determined using a MiniFlex 600 X-ray diffractometer (Rigaku, Japan) coupled with Cu Kα radiation (λ = 1.5406 Å) from 2° to 35° with a speed of 10° min^{-1}.

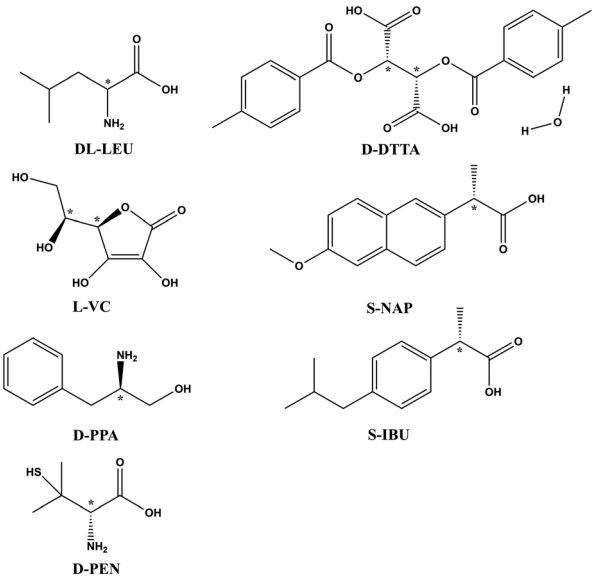

Fig. 1 Molecular structures of DL-LEU and ligands.

Thermal analysis. The melting points of monomers and multi-component crystals were detected by differential scanning calorimetry (Mettler Toledo, DSC1). 5–10 mg of samples were heated from 30 °C to 330 °C at a rate of 5 °C min^{-1} in a pinhole aluminum crucible under a nitrogen protective atmosphere. The thermal stability of the samples was tested using thermogravimetric analysis (Mettler Toledo, Switzerland, TGA). The 5–10 mg samples were heated from 25 °C to 500 °C at a rate of 5 °C min^{-1} under a nitrogen atmosphere.

Fourier Transform Infrared Spectroscopy (FT-IR). The Fourier transform infrared spectra (Bruker Corporation Ltd., Germany) data of DL-LEU, D-/L-LEU, D-DTTA and multi-component crystals were collected using a Bruker Alpha ATR platinum instrument to verify the formation of the new phases. The spectral scanning range was 3500–400 cm^{-1} with a resolution of 4 cm^{-1}. Each sample was scanned a total of 32 times.

Single Crystal X-ray Diffraction (SCXRD). The SCXRD data was obtained using a Rigaku XtaLAB P200 diffractometer with Cu Kα (λ = 1.54184 Å). In Olex2 software,[31] the structure was solved using the intrinsic phase by the SHELXT structure solution program and refined with the SHELXL refinement package using least-squares minimization.[32,33]

Preparation of multi-component single crystals. Two kinds of single crystals, D–D and L–D, were prepared by slow evaporation crystallization. D-LEU and D-DTTA of equal molar ratio were dissolved in MeOH/H_2O at 1 : 1 (v/v), and a good quality single crystal was obtained after 8 mL was slowly volatilized at room temperature for three days. Similarly, L-LEU and D-DTTA were prepared in a saturated solution of MeOH/H_2O at 1 : 1 (v/v), and 8 mL was slowly volatilized at

room temperature for two days to obtain a single crystal with good quality.

Measurement of solubility. The solubility of D–D and L–D in MeOH/H_2O at 1 : 4, 3 : 7, 2 : 3 and 1 : 1 (v/v) was measured at 5 °C intervals in the range of 10–40 °C. The specific steps are as follows: excess solids were added to sample bottles containing 20 mL solvent, respectively, and the mixture was stirred continuously for 24 h to achieve thermodynamic equilibrium. The suspension was left to stand for 3 h. The supernatant was filtered by a 0.45 μm nylon filter membrane, diluted five-fold, and quantified by chiral high performance liquid chromatography (HPLC). The standard curves of D–D and L–D were measured (Fig. S2†). After the solubility test, the undissolved wet solids were examined by PXRD to ensure that no crystal form transformation occurred in the solute during the experiment process.

The concentration of DL-LEU was measured at 254 nm using a UV-vis detector on Waters Alliance 2695, a reversed-phase chromatograph. The samples were measured on an MCI GEL CRS10W chiral column (internal diameter, 4.6 mm; length, 50 mm) with 0.5 mmol L^{-1} $CuSO_4$ aqueous solution at a flow rate of 0.5 mL min^{-1}. The retention time of D-LEU and L-LEU was 14.6 min and 21.6 min, respectively.

***In situ* Raman monitoring.** A Raman spectrometer (ReactRaman 785, Mettler Toledo, America) was used to monitor the D–D and L–D suspension crystallization process at room temperature in the spectral range from 300 cm^{-1} to 1850 cm^{-1}. 3.99 mmol D-LEU was first added to a 50 mL crystallizer containing 25 mL MeOH/H_2O at 2 : 3 (v/v) and stirred with a magnetic agitator at 350 rpm. In a dark environment, the Raman probe was inserted into the suspension at a certain angle for monitoring, and the sampling time was 45 s. Then 3.99 mmol D-DTTA was added and further stirring was performed to monitor the formation of D–D. Similarly, 7.98 mmol L-LEU and 7.98 mmol D-DTTA were added to the crystallizer and the formation of L–D was monitored in the same way.

Molecular simulation. The molecular electrostatic potential (MESP) can be used to show the charge distribution of a molecule and to identify the sites of interaction with other molecules.[34] The geometric optimization of D-LEU, L-LEU and D-DTTA was performed using Gaussian 09D[35] at the B3LYP/6-311+G (d, p) level, respectively. The results were then analyzed and visualized by Multiwfn 3.8 (ref. 36) and VMD 1.9.3 (ref. 37) software.

The intermolecular interactions in D–D and L–D were analyzed by atoms in molecules (AIM) and independent gradient model based on Hirshfeld partition (IGMH). The molecular clusters extracted from single crystal structures were geometrically optimized by Gaussian 09D at the B3LYP/6-311+G (d, p) level. The electron density (ρ), Laplacian electron density ($\Delta^2\rho$) and local energy density parameters (Lagrangian kinetic energy density ($G(r)$), potential energy density ($V(r)$) and energy density ($H(r)$)) at the bond critical point (BCP) were calculated by Multiwfn 3.8 to determine the type of intermolecular interaction and the strength of the hydrogen bond.[38] Finally, VMD 1.9.3 is used for visual analysis. The strength of the hydrogen bond can be calculated according to the following formula:

$$E_H = -223.08 \times \rho_{BCP} + 0.7423 \quad (1)$$

where E_H represents the energy of the hydrogen bond and ρ_{BCP} represents the electron density at BCP.[39]

Then, Multiwfn 3.8 and VMD 1.9.3 were used to draw the IGMH scatter plot and isosurface plot to realize the visualization of weak interactions in molecular systems.[40]

Hirshfeld surface[41] and two-dimensional (2D) fingerprint analysis were performed by CrystalExplorer 17.5 (ref. 42) to visualize and quantitatively characterize intermolecular interactions in multi-component crystals.

The binding energy was calculated by Materials Studio 7.0 software. Using the "Forcite" module, the COMPASS force field was selected to calculate the energy of geometrically optimized synthons and monomers respectively. Then the binding energy of different multi-component crystal synthons was obtained by further calculation.[43] The binding energy was calculated as follows:

$$\Delta E_{bind} = E_{AB} - E_A - E_B \quad (2)$$

where E_{AB} represents the energy of the optimized synthons, and E_A and E_B represent the energy of the optimized monomers.

Materials Studio 7.0 was used to carry out geometric optimization of the synthons in the asymmetric unit. The MeOH/H_2O at 2 : 3 (v/v) solvent box was constructed through the Amorphous Cell module and then the geometric optimization was executed using the COMPASS force field. Molecular dynamics simulations of 1000 ps each were carried out using the NVT and NPT ensembles. The total solvation free energy can be calculated as the sum of the ideal, van der Waals and electrostatic contributions.[44]

Chiral resolution. DL-LEU (1 mmol) and D-DTTA (1 mmol) were dissolved in 20 mL MeOH/H_2O at 2 : 3 (v/v). After adding the D–D seed at 50 °C, cooling crystallization was carried out. After the experiment, the solid and mother liquor were obtained by filtration. The ee value (eqn (3)) of the product was detected by offline HPLC. The effects of the seed amount, cooling rate and end point temperature on the separation efficiency were studied. In order to improve the ee value and yield of the product, multiple cycle crystallization was adopted.

$$ee = \frac{[D] - [L]}{[D] + [L]} \times 100\% \quad (3)$$

Results and discussion

Solid-state characterization

The grinding product of "DL-LEU + D-DTTA" showed new characteristic peaks at 2θ = 7.20°, 7.56°, 12.89°, 13.54°, *etc.*, which were different from those of DL-LEU and D-DTTA,

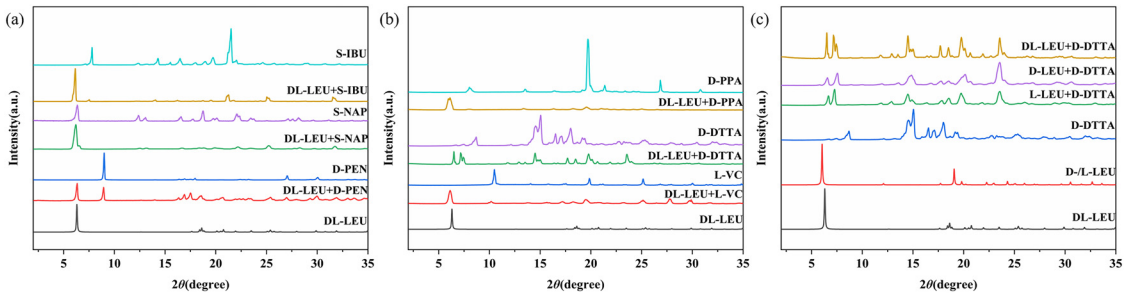

Fig. 2 X-ray powder diffraction data of the grinding product of DL-LEU with *S*-IBU, *S*-NAP and D-PEN (a), the grinding product of D-LEU with D-PPA, D-DTTA and L-VC (b) and the grinding product of D-DTTA with D-LEU, L-LEU and DL-LEU (c).

indicating that new phases are formed after LAG screening (Fig. 2a and b). There were no new peaks in the PXRD spectra of the grinding products between the remaining ligands and DL-LEU, confirming that the other ligands did not form new phases with DL-LEU. As shown in Fig. 2c, the grinding product of "D-LEU + D-DTTA" exhibited new characteristic peaks different from D-LEU and D-DTTA at 2θ = 6.52°, 7.56°, 13.54°, 16.73° and 18.45°. New characteristic peaks of the grinding product of "L-LEU + D-DTTA" appeared at 2θ = 6.65°, 7.20°, 12.89°, 16.37° and 18.51°, which were distinct from those of L-LEU and D-DTTA, indicating the formation of new substances. The PXRD pattern of "DL-LEU + D-DTTA" is the superposition of the PXRD patterns of "D-LEU + D-DTTA" and "L-LEU + D-DTTA", indicating that D-DTTA has a resolution effect on DL-LEU.

The melting points of "D-LEU + D-DTTA" and "L-LEU + D-DTTA" were 167.90 °C and 156.01 °C respectively, and the melting process is accompanied by decomposition, which are different from the parent compounds (301.21 °C and 175.34 °C). This further proved the formation of new substances from the perspective of thermodynamic properties (Fig. 3a). In addition, there were small endothermic peaks in front of the melting point peak of "L-LEU + D-DTTA" and D-DTTA, which is caused by the desolvation of solvates (Fig. 3b).

The infrared spectra of each substance are shown in Fig. 3c. The results show that the characteristic peaks of D-/L-LEU appear at 3052 cm^{-1}, 2990 cm^{-1} to 2868 cm^{-1} and 1607 cm^{-1}, corresponding to the stretching vibration of $-NH_2$, stretching vibration of –OH and bending vibration of $-NH_2$, respectively. The characteristic peaks of D-DTTA appear in the range of 2067 cm^{-1} to 2920 cm^{-1} and 1732 cm^{-1} to 1717 cm^{-1}, which correspond to the stretching vibration of –OH and the stretching vibration of –C═O. After grinding, the characteristic peaks of D-/L-LEU and D-DTTA were shifted to different degrees, indicating that new hydrogen bonds or other non-covalent interactions were formed in the crystals. This change also further verified the formation of new substances.

Structural analyses of D–D and L–D

The crystallographic data of the prepared single crystals are given in Table S2.† Both D-LEU:D-DTTA:0.5H_2O (D–D) and L-LEU:D-DTTA:0.357CH_3OH:0.75H_2O (L–D) crystals were salts with the proton transferred from the carboxyl group in the D-DTTA molecule to the amine group of LEU. The PXRD patterns obtained by single crystal simulation are consistent with those measured in practice (Fig. S3†).

The D–D crystal belongs to the chiral monoclinic space group *C*2. There are eight D-LEU molecules, eight D-DTTA molecules and four H_2O molecules in the unit cell, and the asymmetric unit contains two D-LEU molecules, two D-DTTA molecules and one H_2O molecule. D-DTTA1 is connected with D-LEU1 and D-DTTA2 through N2–H2B···O13, O14–H14···O3 and O14–H14···O4, and D-LEU2 is connected with D-DTTA2 through O18–H18A···O8, respectively. There is an O21–H21E···O1 hydrogen bond between D-DTTA2 and H_2O molecules. The asymmetric elements are connected by N1–H1F···O12 and O6–H6···O11 to form a one-dimensional chain structure, which grows along the *oc* direction (Fig. 5a). The two-dimensional chain is formed by N2–H2A···O9, N2–H2C···O5, N1–H1E···O16, N1–H1D···O4 connections

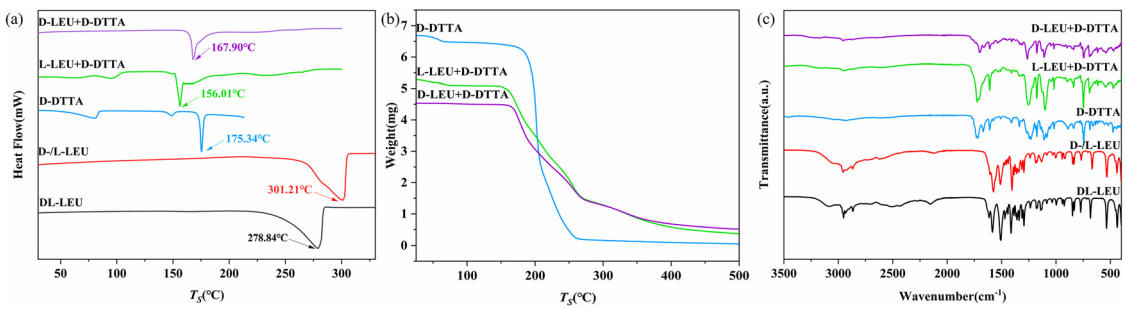

Fig. 3 DSC curves (a), TGA curves (b) and FT-IR patterns (c) of DL-LEU, D-/L-LEU, D-DTTA, the slurry product of D-LEU with D-DTTA and the slurry product of L-LEU with D-DTTA.

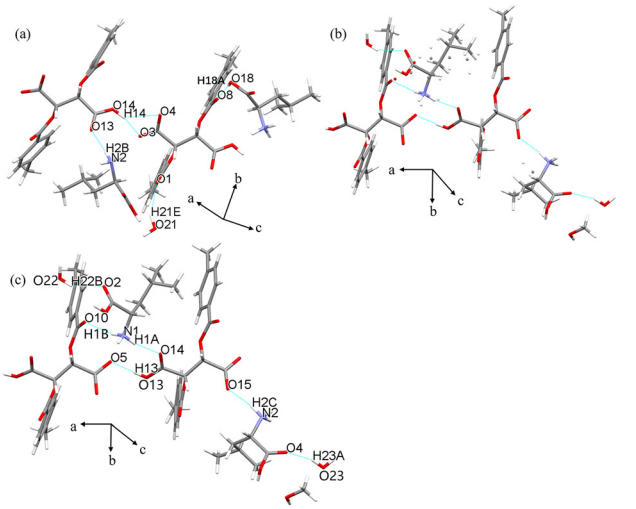

Fig. 4 Asymmetric units of D–D (a), L–D containing disordered structure (b) and disordered structure with high space occupancy L–D (c).

between one-dimensional chains (Fig. 5b). The three-dimensional packing depends on the π–π packing of the benzene ring of the D-DTTA molecule (Fig. 5c).

L–D belongs to the chiral monoclinic *I*2 space group. The unit cell contains eight L-LEU molecules, eight D-DTTA molecules, 1.428 methanol molecules and three H_2O molecules. The asymmetric unit of L–D is composed of two L-LEU molecules, two D-DTTA molecules, 0.357 methanol molecules and 0.75 H_2O molecules. There are three disorders of L-LEU in L–D (Fig. 4b). After that, the analysis of the L–D crystal was carried out according to the situation of large space occupation (Fig. 4c). D-DTTA1 is connected to L-LEU1 and D-DTTA2 by N1–H1B···O10 and O13–H13···O5, respectively. D-DTTA2 is connected to L-LEU1 and L-LEU2 *via* N1–H1A···O14 and N2–H2C···O15, respectively. L-LEU2 is connected to a H_2O molecule *via* O23–H23A···O4, and L-LEU1 is connected to another H_2O molecule *via* O22–H22B···O2. The asymmetric elements are connected by N2–H2A···O12, O8–H8···O16 and O8–H8···O15 to form a one-dimensional chain structure (Fig. 6a). A two-dimensional chain is formed by connecting N2–H2B···O6 and N1–H1C···O7 between one-dimensional chains (Fig. 6b). The three-dimensional structure is formed between layers by π–π stacking of the benzene ring of the D-DTTA molecule (Fig. 6c).

Intermolecular interaction analyses of D–D and L–D

The weak interaction between two kinds of crystals was analyzed by molecular electrostatic potential. The red region of the positive potential represents the nucleophilic position, and the blue region of the negative potential represents the electrophilic position. In general, the darker the color on the MESP, the greater the absolute value of the potential extremum, indicating that the site is more likely to interact. As shown in Fig. 7, for the D-DTTA monomer, the largest positive potential is located near the carboxyl hydrogen atom (+63.49 kcal mol^{-1}). For D/L-LEU monomers, the negative potentials around the carbonyl oxygen atoms are the lowest (−39.54 kcal mol^{-1} and −34.24 kcal mol^{-1}), and the negative potentials around the amino nitrogen atoms are the second lowest (−32.84 kcal mol^{-1} and −33.82 kcal mol^{-1}). D-DTTA has such a high positive potential, suggesting that the hydrogen atoms on the carboxyl group are easily protonated and transferred to another monomer, thus forming a salt rather than a cocrystal.

IGMH was used to analyze the types and regions of intermolecular interactions.[45] All the points in the isosurfaces were collected and plotted as scatter maps. Green represents van der Waals forces, blue represents strong interactions such as hydrogen and ionic bonds, and red represents strong non-bond packing and steric hindrance effects of cages or rings. From Fig. 8, it can be seen that there are blue oblates wrapped in green between the carboxyl

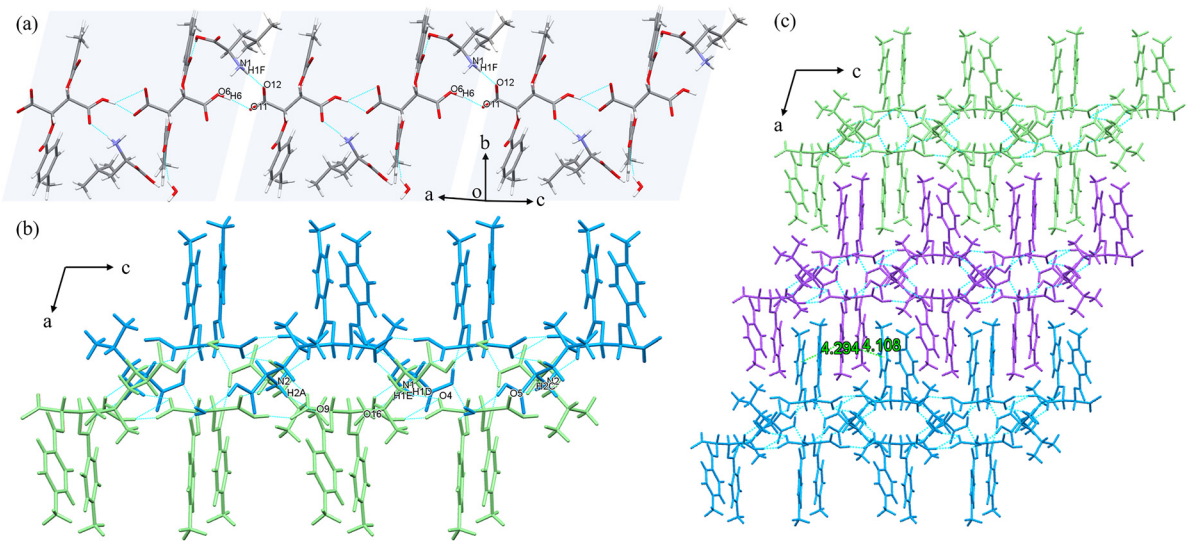

Fig. 5 (a) One-dimensional chain structures of D–D. (b) Two-dimensional chain structures of D–D. (c) Three-dimensional stacked structures of D–D.

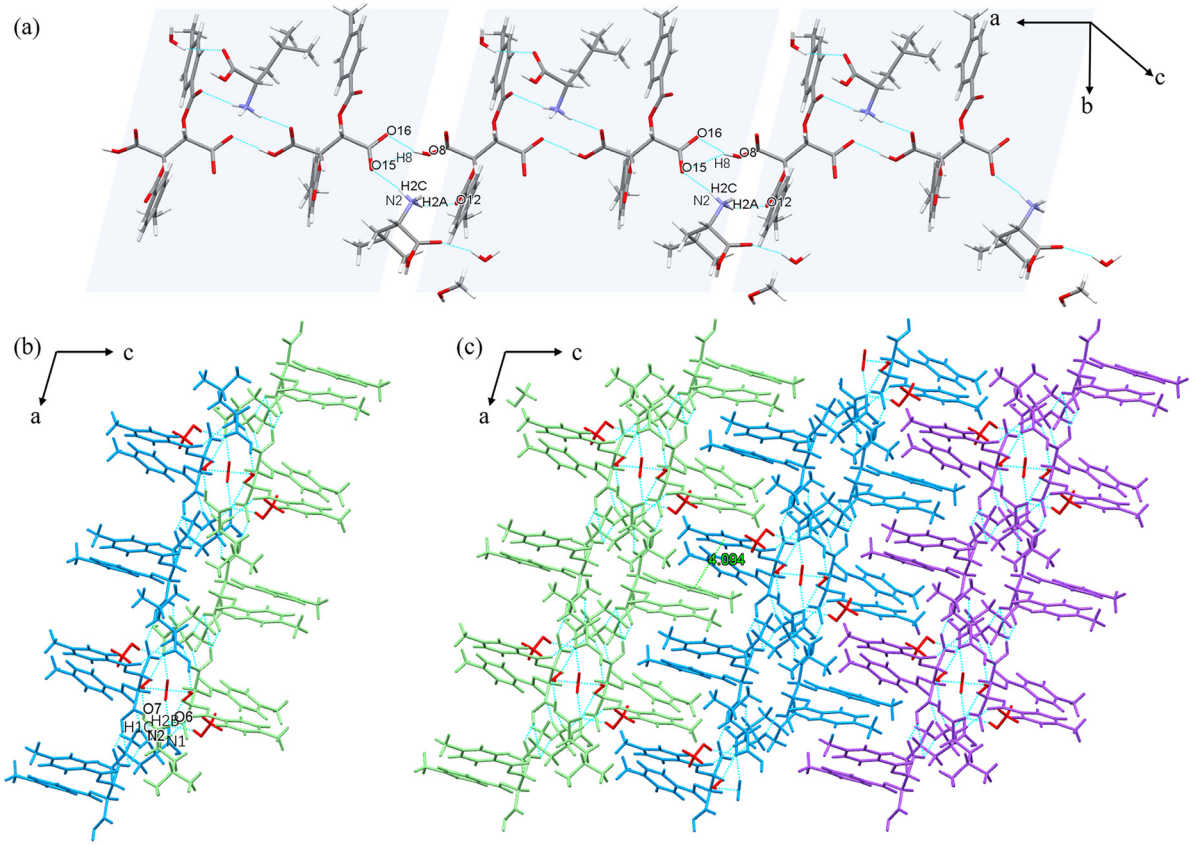

Fig. 6 (a) One-dimensional chain structures of L–D. (b) Two-dimensional chain structures of L–D. (c) Three-dimensional stacked structures of L–D.

group on the DTTA and the surrounding amino group, demonstrating the existence of van der Waals and hydrogen bonding, but blue is dominant, so hydrogen/ionic bonding takes up more proportion. The blue oblate circle between D-DTTA1 and D-DTTA2 has the deepest color, indicating that the force is strongest here. There are also green isoplanes at other locations, reflecting that regions of the overall structure that are not involved in hydrogen bonding are mainly stacked by van der Waals forces.

Hirshfeld surface analysis was applied to reveal the relative contribution percentage of interaction sites, reflecting the intermolecular interaction. Red areas represent strong contacts such as N···H and O···H, white areas represent weak contacts such as C···H, and blue areas indicate the absence of any mutual contact. Since there are two D-DTTA molecules and two LEU molecules in the asymmetric units of D–D and L–D, the Hirshfeld surfaces of these eight molecules are calculated separately. As shown in Fig. 9a and b, the intermolecular hydrogen bonds between the LEU molecule and D-DTTA, N–H···O and O–H···O, appear as red regions on the Hirshfeld surface. Fig. 9c summarizes the percentage contribution of each interaction, with H···H interaction

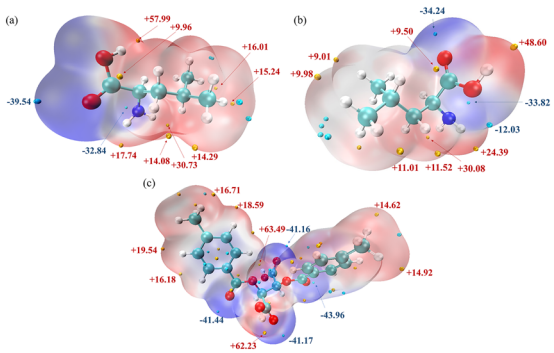

Fig. 7 Analysis of MESP of (a) D-LEU, (b) L-LEU and (c) D-DTTA.

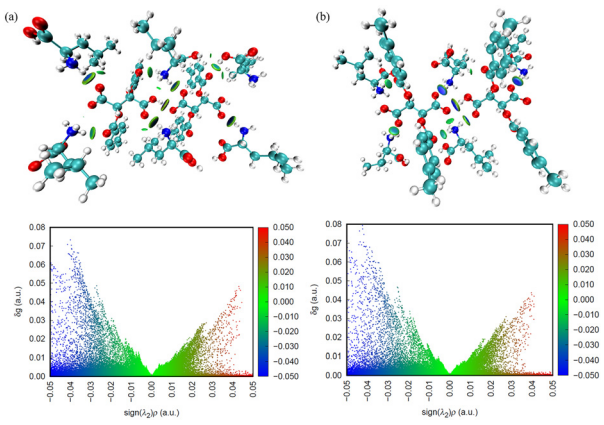

Fig. 8 IGMH isosurfaces and scatter plots of (a) D–D and (b) L–D.

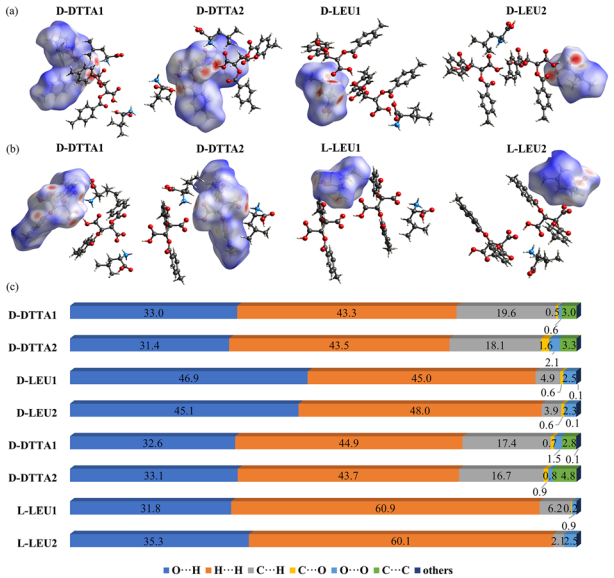

Fig. 9 Hirshfeld surface of D–D (a) and L–D (b). (c) The relative percentage contributions of different intermolecular contacts to the Hirshfeld surface area (from top to bottom, D-DTTA1 in D–D, D-DTTA2 in D–D, D-LEU1 in D–D, D-LEU2 in D–D, D-DTTA1 in L–D, D-DTTA2 in L–D, L-LEU1 in L–D, L-LEU2 in L–D).

accounting for the highest percentage, followed by O···H and C···H contacts, and other interactions with lower proportions. This is consistent with the presence of van der Waals forces in the IGMH analysis. The proportion of O···H interaction increased from 31.8–35.3% around the L-LEU molecule in L–D to 45.1–46.9% around the D-LEU molecule in D–D. The proportion of H···H interaction decreased from 60.1–60.9% around the L-LEU molecule in L–D to 45.0–48.0% around the D-LEU molecule in D–D. The presence of C···C contacts around D-DTTA for both crystals indicates the existence of π–π packing in the crystals. The differences in the interactions between the two crystals demonstrate that the different chiral configurations of the molecules lead to different intermolecular forces during crystal packing.

Thermodynamic properties of D–D and L–D

The solubility of D–D and L–D in MeOH/H_2O at 1 : 4, 3 : 7, 2 : 3 and 1 : 1 (v/v) was measured at 10–40 °C. It can be observed that the PXRD patterns before and after the solubility measurement are consistent, indicating no changes in the crystal forms of D–D and L–D during the solubility measurement process (Fig. S4†). In the range of 10–40 °C, the solubility of D–D and L–D increases with the increase of temperature, and the solubility of L–D is always greater than that of D–D at the same temperature (Fig. 10a). As shown in Fig. 10b, the solubility difference between L–D and D–D in MeOH/H_2O at 2 : 3 (v/v) is the largest at 10 °C, 15 °C, 25 °C and 30 °C. And the final temperature of resolution is generally selected at a low temperature, so MeOH/H_2O at 2 : 3 (v/v) is selected as the solvent. The significant solubility difference laid a good basis for the subsequent separation.

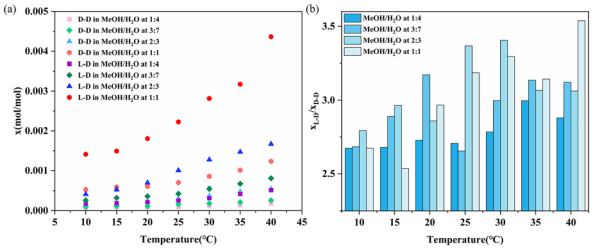

Fig. 10 (a) The mole fraction solubility of D–D and L–D in binary mixed solvents of methanol and water with different ratios; (b) the ratio of the solubility of L–D to that of D–D at different solvents and temperatures.

Selective formation process of the salts

The suspension crystallization process of D–D and L–D at room temperature was monitored by Raman spectroscopy, recording the peak shifts and the appearance of new peaks during the process. For D–D, the peak belonging to D-LEU at 533 cm^{-1} before the reaction disappeared. A new peak, different from the starting material, appeared at 1714 cm^{-1} (Fig. 11a). The variation of the peak intensity at wavenumbers 533 cm^{-1} and 1714 cm^{-1} with time is shown in Fig. 11b. The results pinpointed that the conversion of D–D was completed in 78 min. For L–D, the peak belonging to L-LEU at 533 cm^{-1} disappeared and the peak belonging to D-DTTA at 1282 cm^{-1} shifted to 1278 cm^{-1} (Fig. 11c). The variation of the peak intensity at wavenumbers 533 cm^{-1} and 1278 cm^{-1} with time is shown in Fig. 11d. The transformation of L–D was completed in 2 h 23 min. Therefore, the formation time of D–D is shorter than that of L–D. This reveals the reason why D–D can be formed preferentially from the reaction kinetics.

Resolution mechanism

The hydrogen bond strength at the electrostatic complementary pairing site was studied by AIM (Fig. 12). The

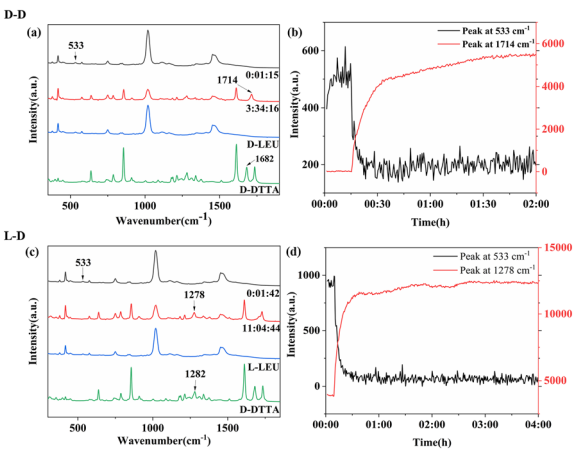

Fig. 11 The results of salt synthesis monitoring by Raman spectroscopy in the spectral range of 300–1850 cm^{-1}. The peak shift (a) and main peak intensity (b) changes in the system consisting of D-LEU and D-DTTA. The peak shift (c) and main peak intensity (d) changes in the system consisting of L-LEU and D-DTTA.

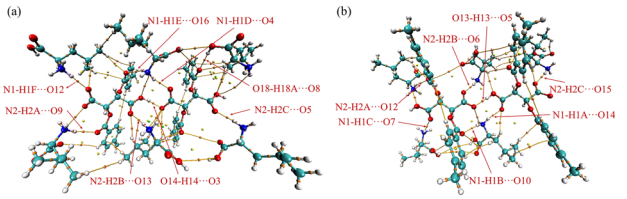

Fig. 12 AIM topology diagrams of D–D (a) and L–D (b).

main types of hydrogen bonds in the crystal structures were analyzed. The average H-bond strength of D–D is −7.2698 kcal mol^{-1}, larger than that of L–D (−6.8850 kcal mol^{-1}). The maximum H-bond strength in D–D (−13.8689 kcal mol^{-1}) was also higher than that in L–D (−12.9352 kcal mol^{-1}). The binding degree of D–D is higher than that of L–D (Tables S5 and S6†).

By calculating the binding energy, it was found that the binding ability of D–D and L–D (−131.02 kcal mol^{-1} and −120.09 kcal mol^{-1}) was much higher than that of DL-LEU (−58.49 kcal mol^{-1}) (Table S7†). This suggests that the introduction of D-DTTA can convert DL-LEU from a racemic compound to a pair of diastereomeric salts. Moreover, the binding energy of D–D is higher than that of L–D, indicating that D–D binds preferentially.

The solvation free energy in MeOH/H_2O at the 2 : 3 (v/v) solvent system is calculated (Table S8†). The average free solvation energy of D–D is −38.205 kcal mol^{-1}, which is higher than L–D (−42.336 kcal mol^{-1}). This corresponds to the difference in solubility between D–D and L–D. The more negative binding energy and the more positive solvation free energy together promote the higher stability and lower solubility of D–D, causing it to be preferentially precipitated in the resolution process.

Chiral resolution

The equimolar resolution experiment was carried out in MeOH/H_2O at 2 : 3 (v/v). The effects of the seed amount, cooling rate and end point temperature on the separation effect were investigated. As shown in Fig. S6,† the optimal separation conditions were determined as 10.3 mg seed amount, 0.3 °C min^{-1} cooling rate and 10 °C end point temperature, which kept the solid ee value at 41.08% and the yield at 55.1%. The solid phases and the liquid phases were crystallized several times (Table 1). The ee value of the second cycle crystallization product is 72.24% and the yield is 51.5%, and the ee value of the third cycle crystallization product is 91.20% and the yield is 52.0%. After these three cycles, the product D–D with an ee value of 91.2% was obtained, and the total yield was 15%. Since the ee value of the filtrate obtained from the third cycle is close to the ee value of the solid phase obtained from the second cycle, the two are mixed and the crystallization process is continued. Therefore, with the increase of the number of cycles, the yield will also increase accordingly. The filtrate obtained in the first cycle was cooled and crystallized to obtain the filtrate with an ee value of −57.10%, and then cooled again to obtain the filtrate with an ee value of −73.32%. Then, the solid product L–D with an ee value of −73.32% was obtained by a rotary evaporator, with a total yield of 33.1%.

Table 1 Results of chiral resolution experiment cycles on D–D and L–D

	D–D			L–D		
Cycle	ee_s[a]	ee_l[b]	Yield[c]	ee_s[a]	ee_l[b]	Yield[c]
1	41.08%	−38.71%	55.1%			
2	72.24%	9.88%	51.5%	−7.98%	−57.10%	9.7%
3	91.20%	71.04%	52.0%	−28.02%	−73.32%	18.4%

[a] ee of the solid. [b] ee of the mother liquor. [c] Yield of the solid product relative to the mass of the step.

Conclusions

In this work, the chiral resolution of DL-LEU was carried out using D-DTTA, and the multi-component salts D-LEU:D-DTTA:0.5H_2O and L-LEU:D-DTTA:0.357CH_3OH:0.75H_2O were successfully prepared, which were confirmed by PXRD, DSC, TGA, FT-IR and SCXRD. The mechanism of the selective recognition and resolution of DL-LEU by D-DTTA is then revealed from the perspective of thermodynamics and molecular dynamics. D–D has higher stability and lower solubility. Raman spectroscopy was used to investigate the self-assembly process of D–D and L–D, and the results showed that D–D and L–D were completely transformed in 78 min and 2 h 23 min, respectively. Then, MESP, AIM, IGMH, HS and binding energy reveal the difference between the intermolecular forces of D–D and L–D crystals. Compared with L-LEU, D-DTTA and D-LEU bind more strongly. The solvation free energy further proves the lower solubility of D–D in MeOH/H_2O at 2 : 3 (v/v). Therefore, D–D prefers to precipitate preferentially during the resolution process. Finally, cyclic crystallization was attempted in MeOH/H_2O at 2 : 3 (v/v) and products with high ee values were successfully obtained.

Data availability

Crystallographic data for D–D and L–D has been deposited at the CCDC under 2387200 and 2387201.

Author contributions

Linlin Shi: writing-original draft, methodology, investigation, conceptualization. Zhiqiang Guo: methodology, project administration. Xiaofang Luo: visualization, supervision. Lingli Hou: data curation, formal analysis. Hongchang Wu: validation, data curation. Ruiyu De: validation, investigation. Xin Huang: writing-review & editing, validation. Ting Wang: writing-review & editing, validation. Hongxun Hao: writing-review & editing, supervision. Na Wang: writing-review & editing, funding acquisition. Lina Zhou: writing-review & editing, funding acquisition.

Conflicts of interest

There are no conflicts to declare.

Acknowledgements

This work was supported by the National Natural Science Foundation of China [No. 22108196] and Tianjin Natural Science Foundation [No. 23JCYBJC01450].

Notes and references

1 W. Jiang and B. Fang, *Appl. Biochem. Biotechnol.*, 2020, **192**, 146–179.
2 J. Gal and P. Cintas, *Top. Curr. Chem.*, 2012, **333**, 1–40.
3 F. Fan, H. Yuan, S. Wu, J. Zhai, F. Liu, L. Zhang, X. Liu and J. Lu, *J. Chem. Thermodyn.*, 2020, **140**, 105905.
4 E. Soleimani, H. Alinezhad, M. D. Ganji and M. Tajbakhsh, *J. Mater. Chem. B*, 2017, **5**, 6920–6929.
5 S. Yang, F. Wu, F. Yu, L. Gu, H. Wang, Y. Liu, Y. Chu, F. Wang, X. Fang and C. Ding, *Anal. Chim. Acta*, 2021, **1184**, 339017.
6 D. Wang, J. Lu, L. Zhang, F. Fan, L. Zhang, X. Liu, H. Yuan and X. Zhu, *Ind. Eng. Chem. Res.*, 2020, **59**, 21957–21968.
7 E. A. Walker, M. J. Tiano, S. I. Benyas, L. A. Dykstra and M. J. Picker, *Psychopharmacology*, 1999, **144**, 45–53.
8 H. Lorenz and A. Seidel-Morgenstern, *Angew. Chem., Int. Ed.*, 2014, **53**, 1218–1250.
9 X. Qin, Y. Xu, B. Lou, C. Liu, L. Zhang, X. Liu, H. Yuan, Y. Zhang and J. Lu, *Cryst. Growth Des.*, 2023, **23**, 4607–4620.
10 J. Cao, B. Lou, Y. Xu, X. Qin, H. Yuan, L. Zhang, Y. Zhang, S. Rohani and J. Lu, *ACS Omega*, 2022, **7**, 19828–19841.
11 T. Miao, X. Cheng, Y. Guo, Z. Gong and Z. Wei, *Giant*, 2023, **14**, 100161.
12 H. Bao, Y. Chen and X. Yang, *Angew. Chem., Int. Ed.*, 2023, **62**, e202300481.
13 K. Yabu, S. Masumoto, S. Yamasaki, Y. Hamashima, M. Kanai, W. Du, D. P. Curran and M. Shibasaki, *J. Am. Chem. Soc.*, 2001, **123**, 9908–9909.
14 F. Fan, H. Yuan, Y. Feng, F. Liu, L. Zhang, X. Liu, X. Zhu, W. An, S. Rohani and J. Lu, *Cryst. Growth Des.*, 2019, **19**, 5882–5895.
15 L. Pasteur, *Ann. Chim. Phys.*, 1848, **24**, 442–459.
16 J. Sui, N. Wang, J. Wang, X. Li, J. Yang, Y. Liu, Y. Zhao, X. Huang, T. Wang, L. Zhou and H. Hao, *Cryst. Growth Des.*, 2022, **22**, 4382–4395.
17 Y. Teng, C. Gu, Z. Chen, H. Jiang, Y. Xiong, D. Liu and D. Xiao, *Chirality*, 2022, **34**, 1094–1119.
18 L. Zhang, Y. Xu, B. Lou, X. Qin, L. Zhang, X. Liu, H. Yuan, Y. Zhang, S. Rohani and J. Lu, *Cryst. Growth Des.*, 2022, **22**, 2392–2406.
19 K. PetrušEvska-Seebach, A. Seidel-Morgenstern and M. P. Elsner, *Cryst. Growth Des.*, 2011, **11**, 2149–2163.
20 M. Ciriani, R. Oliveira and C. Afonso, *Green Chem.*, 2022, **24**, 4328–4362.
21 J. Qi, K. Zhang, J. Han, J. Li, H. Zhang and J. Chen, *Chem. Ind. Eng.*, 2023, **40**, 138–146.
22 L. Wang, N. Wang, J. Sui, S. Sun, Z. Feng, G. Li, H. Hao and L. Zhou, *Cryst. Growth Des.*, 2023, **23**, 5641–5650.
23 O. Sánchez-Guadarrama, F. Mendoza-Navarro, A. Cedillo-Cruz, H. Jung-Cook, J. I. Arenas-García, A. Delgado-Díaz, D. Herrera-Ruiz, H. Morales-Rojas and H. Höpfl, *Cryst. Growth Des.*, 2015, **16**, 307–314.
24 L. He, Z. Liang, G. Yu, X. Li, X. Chen, Z. Zhou and Z. Ren, *Cryst. Growth Des.*, 2018, **18**, 5008–5020.
25 J. Kenchel, A. Vázquez-Salazar, R. Wells, K. Brunton, E. Janzen, K. M. Schultz, Z. Liu, W. Li, E. T. Parker and J. P. Dworkin, *Nat. Commun.*, 2024, **15**, 7980.
26 M. Ozaki, T. Nakade, M. Shimotsuma, A. Ikeda, T. Kuranaga, H. Kakeya and T. Hirose, *J. Chromatogr., B*, 2024, **1244**, 124239.
27 K. Yao, Y. Duan, F. Li, B. Tan, Y. Hou, G. Wu and Y. Yin, *Trends Pharmacol. Sci.*, 2016, **37**, 714–727.
28 A. L. Hartman, P. Santos, K. J. O'Riordan, C. E. Stafstrom and J. M. Hardwick, *Neurobiol. Dis.*, 2015, **82**, 46–53.
29 R. Yoshioka, K. Okamura, S. I. Yamada, K. I. Aoe and T. Date, *Bull. Chem. Soc. Jpn.*, 1998, **71**, 1109–1116.
30 O. Shemchuk, E. Spoletti, D. Braga and F. Grepioni, *Cryst. Growth Des.*, 2021, **21**, 3438–3448.
31 O. V. Dolomanov, L. J. Bourhis, R. J. Gildea, J. A. K. Howard and H. Puschmann, *J. Appl. Crystallogr.*, 2009, **42**, 339–341.
32 G. M. Sheldrick, *Acta Crystallogr., Sect. A:Found. Crystallogr.*, 2008, **64**, 112–122.
33 G. M. Sheldrick, *Acta Crystallogr., Sect. A:Found. Adv.*, 2015, **71**, 3–8.
34 S. Anila, *Acc. Chem. Res.*, 2023, **56**, 1884–1895.
35 M. J. Frisch, H. B. Schlegel, G. E. Scuseria, M. A. Robb, J. R. Cheeseman, V. Barone and B. Mennucci, *Gaussian 09, Revision A.02*, Gaussian, Inc., Wallingford, CT, 2009.
36 T. Lu and F. Chen, *J. Comput. Chem.*, 2012, **33**, 580–592.
37 W. Humphrey, A. Dalke and K. Schulten, *J. Mol. Graphics*, 1996, **14**, 33–38.
38 R. F. W. Bader, *Chem. Rev.*, 1991, **91**, 893–928.
39 S. Emamian, T. Lu, H. Kruse and H. Emamian, *J. Comput. Chem.*, 2019, **40**, 2868–2881.
40 T. Lu and Q. Chen, *J. Comput. Chem.*, 2022, **43**, 539–555.
41 L. D. Prado, A. B. X. Santos, H. V. A. Rocha, G. B. Ferreira and J. A. L. C. Resende, *Int. J. Pharm.*, 2018, **553**, 261–271.
42 D. Jayatilaka, S. K. Wolff, D. J. Grimwood, J. J. Mckinnon and M. A. Spackman, *Acta Crystallogr., Sect. A:Found. Crystallogr.*, 2006, **62**, s90.
43 S. F. Boys and F. Bernardi, *Mol. Phys.*, 1970, **19**, 553–566.
44 R. L. Wolfenden, L. Andersson, P. M. Cullis and C. C. B. Southgate, *Biochemistry*, 1981, **20**, 849–855.
45 T. Lu and Q. Chen, *ChemRxiv*, 2021, preprint, DOI: **10.26434/chemrxiv-2021-628vh**.